A Monolithically Integrable Reconfigurable Antenna Based on Large-Area Electronics

Can Wu, *Student Member, IEEE*, Yue Ma, *Graduate Student Member, IEEE*,
Suresh Venkatesh, *Senior Member, IEEE*, Yoni Mehlman, *Student Member, IEEE*,
Murat Ozatay, *Member, IEEE*, Sigurd Wagner, *Life Fellow, IEEE*,
James C. Sturm, *Life Fellow, IEEE*, and Naveen Verma, *Senior Member, IEEE*

Abstract— **Reconfigurable antennas introduce unique and dynamic system capabilities for wireless communication and sensing, by enabling controllable radiation pattern, frequency response, and polarization of electromagnetic (EM) waves. The antenna's physical dimensions are critical to enhancing control of radiative characteristics, making it necessary to distribute RF control devices across a large-area aperture. Previous reconfigurable antennas have been limited in scale and performance by the need to assemble discrete active components. Large-area electronics (LAE) is a technology that can enable monolithic reconfigurable antennas, with flexible and large form factors. However, conventionally the speed of LAE, specifically of thin-film transistors (TFTs), has been restricted to 10–100 MHz. In this work, a reconfigurable antenna based on LAE RF TFTs is achieved through a combination of: 1) materials and device enhancements pushing fundamental TFT performance metrics to the giga-Hertz regime and 2) an architecture that employs the TFTs as passive switches, rather than active amplifiers, to enable aggressive biasing for high-frequency operation, yet within the breakdown limits. A 9×9 cm^2 reconfigurable antenna consisting of an 11×11 array of metal patches as sub-radiators controlled by 208 TFT-based RF switches is demonstrated. Far-field and *S*-parameter measurements show reconfigured beam steering by 90° and resonant-frequency tuning by 200 MHz.**

Index Terms— **Internet of Things (IoT), large-area electronics (LAE), reconfigurable antenna, thin-film transistor (TFT), wireless sensing.**

I. INTRODUCTION

THE Internet of Things (IoT) envisions a large number of widely and densely distributed sensing devices, which are typically accessed using low-power giga-Hertz radios [1], [2], [3]. As illustrated by the example of a smart warehouse in Fig. 1, the dense and spatial nature of the network requires
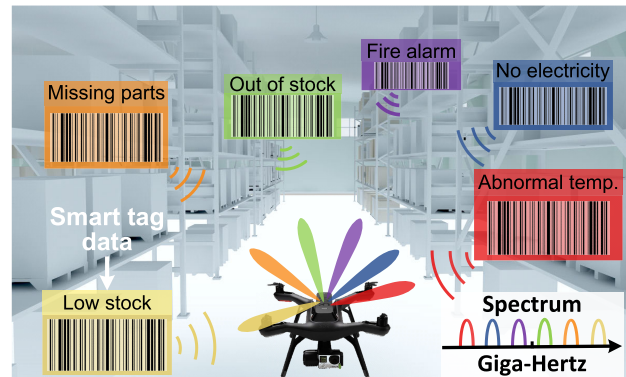
Fig. 1. IoT systems envision antennas with dynamically tunable beam directionality and frequency.

several critical functionalities for wireless accessing, including direction finding, addressing, and transmission, as well as flexible spectrum allocation and polarization control. Such agility presents significant new opportunities and challenges for antennas, which serve as the interface between guided signals in the system and unguided electromagnetic (EM) waves to the distributed nodes. The constraints of traditional designs with fixed parameters motivate a new class of antennas, with designs where the key parameters, such as directionality, frequency response, and polarization, can be reconfigured.

Such parameter reconfigurability can be achieved by setting the RF current distribution across the radiating aperture, using controllable devices [4], [5], [6], [7], [8], [9], [10], [11], [12], [13], [14], [15], [16]. Moreover, there is significant interest in creating physically large apertures (cm's to m's), as this enhances reconfigurability, directionality, and radiation efficiency. Large antennas are particularly important for communication in the low-power sensing band of 2.4 GHz ($\lambda = 12.5$ cm in vacuum/free space) [17], [18], [19]. Up to now, antenna size for this band has been limited by the lack of a technology offering control devices with adequate RF performance over the centimeter-to-meter dimensions required [4], [7]. All reconfigurable-antenna realizations thus far have employed assembly of discrete devices [4], [5], [6], [7], [8], [9], [10], [11], [12], [13], [14], [15], [16], limiting performance and cost for widescale IoT applications.

Large-area electronics (LAE) is a compelling candidate technology for IoT. LAE employs monolithic integration of semiconductors, metals, and dielectrics over meter-scale
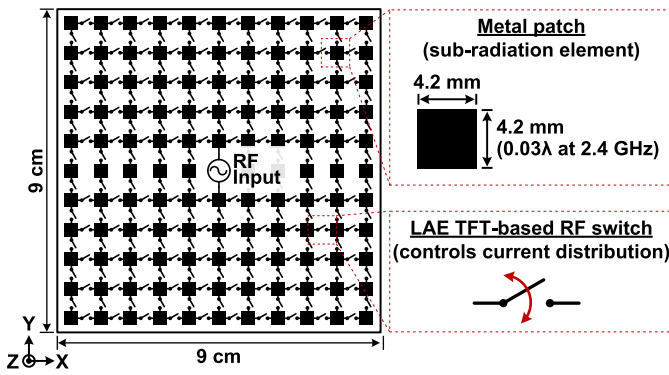
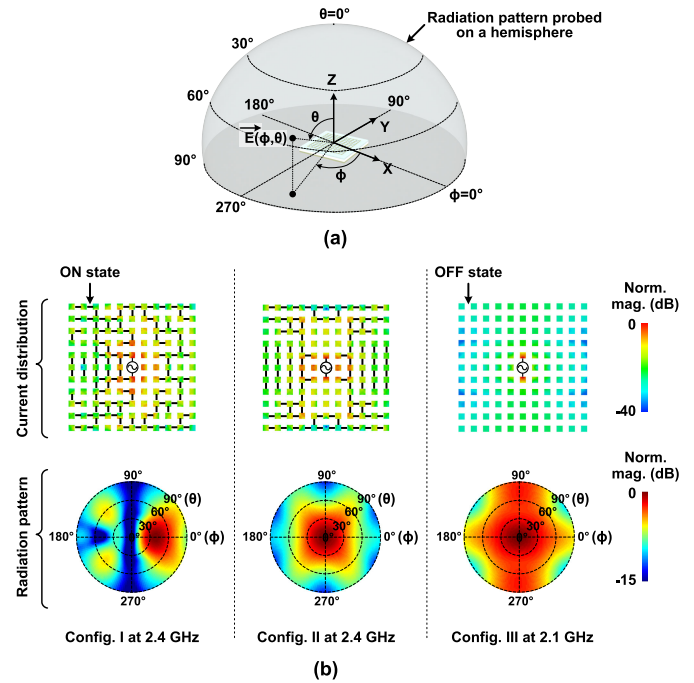Fig. 2.   Architecture of the reconfigurable antenna.

Fig. 3.   Full-wave EM simulation of the reconfigurable antenna for three representative switch configurations. (a) Definition of coordinate axes. (b) Simulated antenna characteristics. In the current-distribution heat maps (top), thick black lines indicate where switches are ON, while their absence indicates where switches are OFF.

dimensions at low cost on rigid or flexible substrates [20], [21], [22], [23], [24], [25], [26], [27], [28]. The primary application of LAE has been flat-panel displays, with industrial fabrication on up to 10 m^2 glass or plastic substrates [29]. Such dimensions and substrates require low-temperature fabrication processing and technologies, resulting in low charge-carrier mobilities that have restricted LAE system frequencies to 10's of mega-Hertz [26], [30], [31], [32], [33], [34], far below the frequencies required for practical wireless systems.

Here we expand on the initial report [35] of the first demonstration of a monolithically-integrable reconfigurable antenna based on LAE, suitable for IoT wireless systems operating in the 2.4 GHz band. The radiating aperture is formed by a 2-D array of metal patches on a flat substrate. Reconfigurability is achieved via LAE thin-film-transistor (TFT)-based RF switches placed between neighboring patches. The ON/OFF states of the switches control the current distribution across the antenna aperture, thus setting its radiative characteristics. The operating frequency of commercial LAE TFTs is inadequate for giga-Hertz applications. By systematic device and circuit co-design, we boost the operating frequency of TFT switches to enable LAE technology in the giga-Hertz regime. This provides an approach to implementing monolithic reconfigurable antennas that can scale to large physical dimensions, enabling wireless capabilities impracticable by conventional technologies (e.g., Si, RF-micro-electromechanical systems (MEMS), and III–V's) [4], [5], [6], [7], [8], [9], [10], [11], [12], [13], [14], [15], [16].

II. SYSTEM ARCHITECTURE

The design of our reconfigurable antenna is shown in Fig. 2. The radiating aperture has a size of 9×9 cm^2 and consists of an 11×11 array of uniformly spaced square metal patches, each 4.2 mm on a side. Between two neighboring patches, a TFT-based RF switch is placed to configure direct current paths across the array. The RF input is fed into the antenna via two central patches. The entire design can be implemented as a multilayer planar structure of thin-film dielectrics, semiconductors, and metals. We adopt standard manufacturing techniques of the LAE flat-panel display industry, wherein the thin films can be deposited onto a glass or plastic substrate and lithographically patterned, all at low temperatures (<200 °C) [21], [30], [31], [32], [33], [34].

Each metal patch acts as a sub-radiator. In its vicinity, the EM field is controlled by: 1) current directly flowing in from its neighbors through RF switches and 2) surface current induced by interactions with nearby patches via near-field coupling. Hence, the overall characteristics of the antenna, including electrical impedance (seen by the RF source), far-field polarization, and radiation pattern, are controlled by the combined ON/OFF states of the switches in the array.

To analyze these characteristics, full-wave 3-D EM simulations are performed using a time-domain solver based on the finite integration technique provided by the Computer Simulation Technology (CST) Microwave Studio software package [36]. Fig. 3 shows the current distributions and radiation patterns for three representative switch-state configurations. The coordinates are defined as follows: the antenna is placed on the *xy* plane; the radiation patterns are probed on a hemisphere in the far-field and are shown on a 2-D map using polar coordinates (θ and ϕ).

The different current distributions set the controllable antenna parameters. First, they establish the effective radiating aperture, whose size determines the frequency at which underlying electric fields form standing waves, thereby controlling the antenna's resonant frequency [37]. Second, they establish the electric field, through the relationship given by the inhomogeneous Helmholtz equation between vector potential and current, thus controlling the far-field radiation pattern [37]. Third, they determine the direction of current flow, which also directly sets the polarization of the electric field in the far-field. As examples, Configs. I and II demonstrate antenna reconfigurability in beam direction, and Configs. II and III demonstrate reconfigurability in frequency.
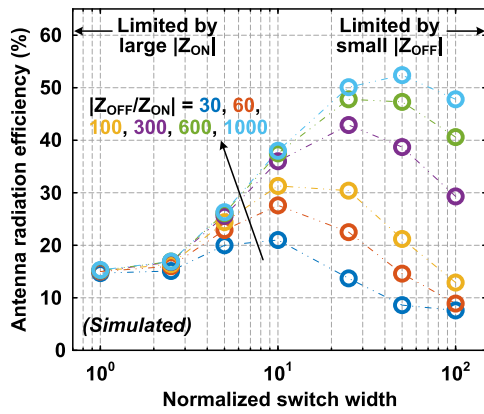
Fig. 4. Simulated reconfigurable antenna radiation efficiency versus normalized switch width. The tradeoff between insertion loss (large $|Z_{ON}|$) and isolation loss (small $|Z_{OFF}|$) leads to an optimal switch width for any $|Z_{OFF}/Z_{ON}|$ ratio.
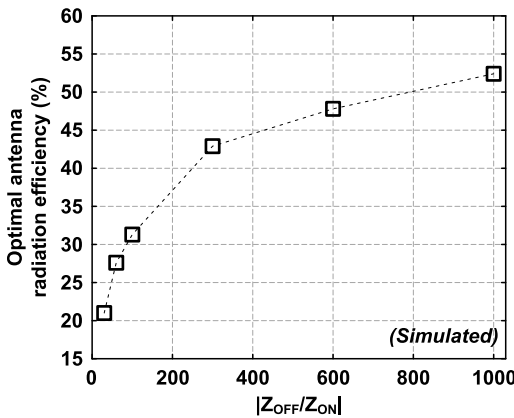

Fig. 5. Optimal antenna radiation efficiency versus $|Z_{OFF}/Z_{ON}|$. The data points are the maximum efficiency values of the curves in Fig. 4.

III. DESIGN OF LAE TFT RF SWITCH

Efficient RF switches operating at giga-Hertz frequencies are the essential components for the reconfigurable antenna. The nonzero impedance of the switch ON state $|Z_{ON}|$ causes insertion loss, and its finite impedance of the OFF state $|Z_{OFF}|$ causes isolation loss, both resulting in system losses. Fig. 4 illustrates their effect by plotting the antenna radiation efficiency versus normalized width of switches implemented for a range of impedance ratios $|Z_{OFF}/Z_{ON}|$ (noting that $|Z_{OFF}|$ and $|Z_{ON}|$ scale together with the chosen switch size). Due to the tradeoff between insertion loss, caused by large $|Z_{ON}|$ (small switch width), and isolation loss, caused by small $|Z_{OFF}|$ (large switch width), an optimal width is observed for radiation efficiency, with the highest achievable efficiency shown in Fig. 5 set by the impedance ratio. Figs. 4 and 5 thus show that the switch impedance ratio $|Z_{OFF}/Z_{ON}|$ is a fundamental metric for reconfigurable antenna system efficiency.

The $|Z_{OFF}/Z_{ON}|$ of LAE TFTs is limited by high parasitic capacitance (sets $|Z_{OFF}|$) and low charge-carrier mobility (sets $|Z_{ON}|$). High parasitic capacitance originates in the TFT source(S)/drain(D)-to-gate(G) overlaps, which in standard TFTs typically range from 10 to 20 μm [21], [22], [38]. The comparatively low electron field-effect mobility originates in trap states in the low-temperature semiconductor materials
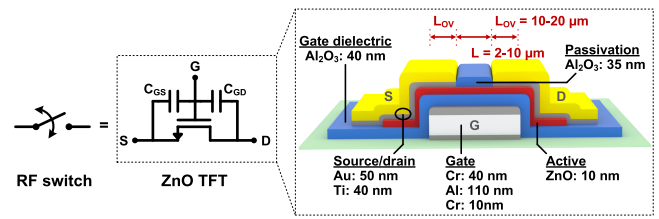

Fig. 6. Schematic of a standard (non-self-aligned) bottom-gate n-channel ZnO TFT with parasitic capacitances.
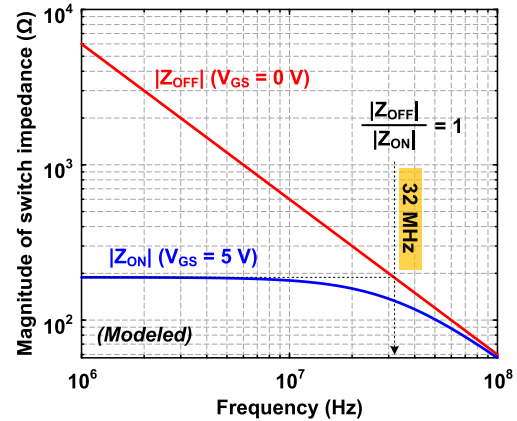

Fig. 7. Modeled impedance of a non-self-aligned ZnO TFT used as an RF switch. While $|Z_{OFF}|$ is dominated by the S/D-to-G overlap capacitances, $|Z_{ON}|$ is dominated by the channel conductance.
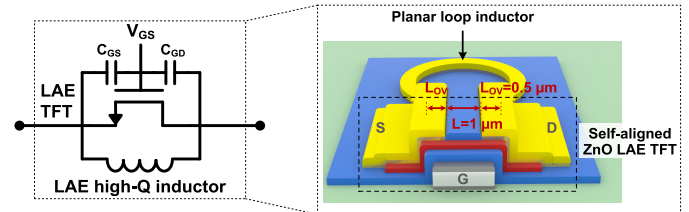

Fig. 8. Resonant LAE RF switch, consisting of a self-aligned ZnO TFT with minimized S/D-to-G overlaps, high-quality-factor LAE inductor, and low-loss thick gate-metal stack, used with high gate-biasing for breakdown-safe passive operation.

used, and typically ranges from 10 to 20 cm^2/V·s in the state-of-the-art LAE TFTs [21], [39].

Fig. 6 illustrates the zinc oxide (ZnO)-based TFT fabricated in our laboratory, in the standard non-self-aligned bottom-gate configuration. The semiconductor (ZnO), gate oxide (Al$_2$O$_3$), and passivation (Al$_2$O$_3$) are deposited by plasma-enhanced atomic layer deposition (PEALD) at a flex-compatible temperature of 200 °C [38]. Typical TFT parameters are: n-channel field-effect mobility of $\sim$20 cm^2/V · s; Al$_2$O$_3$ gate insulator thickness of 40 nm; state-of-the-art channel length of $L = 2$ μm; and S/D-to-G overlap of $L_{OV} = 10$ μm.

The modeled impedances of this TFT, used as an RF switch, are shown in Fig. 7. Its OFF-to-ON impedance ratio drops to unity at a cut-off frequency of 32 MHz, far below the frequency required for a 2.4 GHz reconfigurable antenna.

To enable giga-Hertz reconfigurable antennas, we enhance the TFT $|Z_{OFF}/Z_{ON}|$ via device, circuit, and system architecture co-design, as shown in Fig. 8: we 1) leverage self-aligned TFTs, to reduce the overlap capacitances and enable aggressive
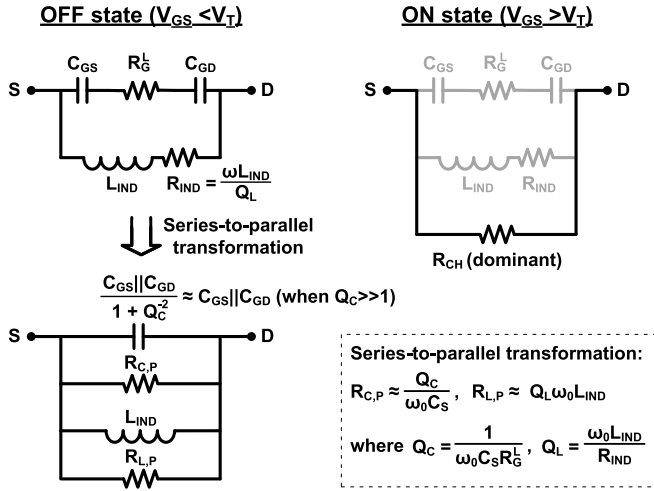
Fig. 9. Circuit model of the resonant RF switch.

Fig. 10. OFF impedance $|Z_{\text{OFF}}(\omega)|$ of the resonant switch versus frequency, for a range of inductor quality factors Q_L.

Fig. 11. Switch OFF impedance $|Z_{\text{OFF}}(\omega_0)|$ (left axis) and bandwidth at half-maximum (right axis) versus inductor quality factor Q_L.

scaling of channel length [40]; 2) resonate out the OFF-state capacitances via a high-quality-factor (high-Q) planar inductor, made possible by the large surface area available in LAE; 3) increase the resonant-circuit quality factor by reducing TFT gate-electrode losses, via thick low-resistance gate-metal materials; and 4) reduce TFT ON-state resistance by aggressive gate biasing while maintaining adequate margin against TFT thermal breakdown, made possible by the passive switch operation required in the antenna architecture.

A. Circuit Model and Optimization of the Resonant Switch

Fig. 9 illustrates the circuit model of the resonant RF switch. The TFT's OFF state is dominated by a parasitic conduction path through the two S/D-to-G overlap capacitors C_{GS} and C_{GD} in series with the gate electrode resistor R_G^L (the superscript "L" represents the gate resistance in the channel length direction, to distinguish it from the traditional definition of the gate resistance along the channel width direction). The TFT's ON state is dominated by the channel conductance $1/R_{\text{CH}}$.

By putting a high-Q inductor L_{IND} in parallel with the TFT, the capacitors can be resonated out at the frequency of interest ω_0, which is 2.4 GHz in our case
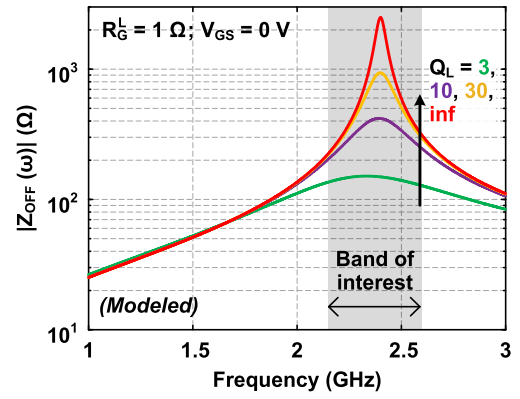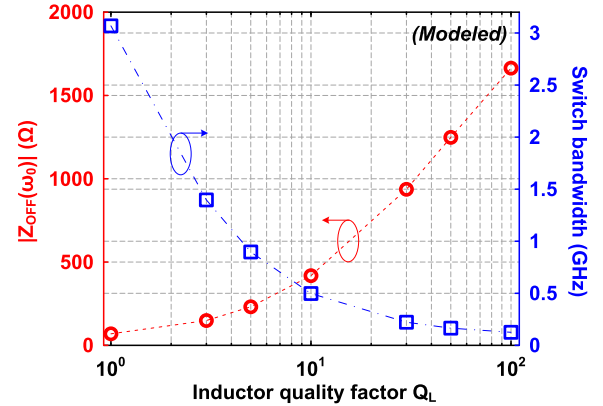
$$\omega_0 = \frac{1}{\sqrt{L_{\text{IND}} C_S}} = 2\pi \cdot 2.4 \text{ GHz}. \tag{1}$$

C_S is the combined capacitance of the two overlap capacitors C_{GS} and C_{GD} in series, i.e., $C_S = C_{\text{GS}}||C_{\text{GD}}$. In the equivalent parallel network, this resonant operation leaves two residual resistances, $R_{C,P}$ and $R_{L,P}$. Their values are set by the capacitance and the quality factors of the inductor and the capacitor

$$R_{C,P} \approx \frac{Q_C}{\omega_0 C_S} \tag{2}$$

$$R_{L,P} \approx Q_L \omega_0 L_{\text{IND}} = \frac{Q_L}{\omega_0 C_S}. \tag{3}$$

Q_C and Q_L are the quality factors of the capacitor and inductor, defined as $Q_C = (1/(\omega_0 C_S R_G^L))$ and $Q_L = ((\omega_0 L_{\text{IND}})/R_{\text{IND}})$.

Therefore, the overall OFF impedance is

$$|Z_{\text{OFF}}| = R_{C,P}||R_{L,P} = \frac{1}{\omega_0(C_{\text{GS}}||C_{\text{GD}})} \cdot (Q_C||Q_L). \tag{4}$$

Thus to boost $|Z_{\text{OFF}}|$, we 1) enhance the quality factors by employing low-loss inductors and a thick, composite gate electrode (Section III-C) and 2) minimize the overlap capacitances C_{GS} and C_{GD} by a self-aligned fabrication process (Section III-D).

B. Bandwidth Versus OFF-Impedance Tradeoff

Fig. 10 shows the OFF-state impedance of the switch $|Z_{\text{OFF}}|$, for four values of the inductor quality factor Q_L. The resonant operation is seen to trade off bandwidth for $|Z_{\text{OFF}}|$. For a fixed gate resistance of $R_G^L = 1$ Ω, Fig. 11 shows the effect of varying Q_L on $|Z_{\text{OFF}}|$ and bandwidth. Raising Q_L from 10 to 30 raises $|Z_{\text{OFF}}|$ by a factor of 2.2, while the bandwidth at half-maximum of $|Z_{\text{OFF}}|$ reduces by 55%. This bandwidth-impedance tradeoff is acceptable in IoT applications, because antennas are typically operated within a narrow bandwidth, to attain high system efficiency [1], [3], [41].

C. High Quality-Factor Inductor and Low-Resistance Gate

Equation (4) suggests that the OFF impedance can be increased by increasing the quality factors of the inductor Q_L and the capacitor Q_C.
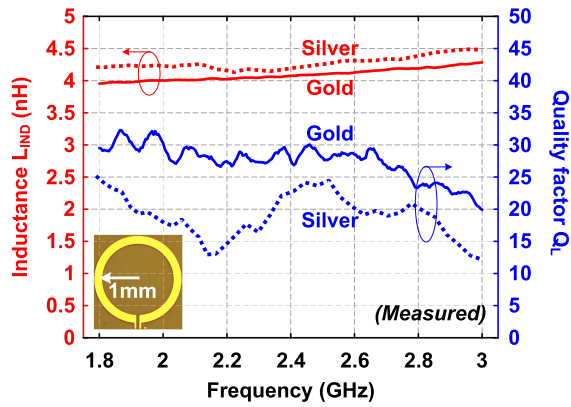
Fig. 12. Measured inductance L_{IND} (left axis) and quality factor Q_L (right axis) of integrated ON-chip planar loop inductors made of 2.5 μm-thick gold and silver. Inset: die photograph of the inductor.
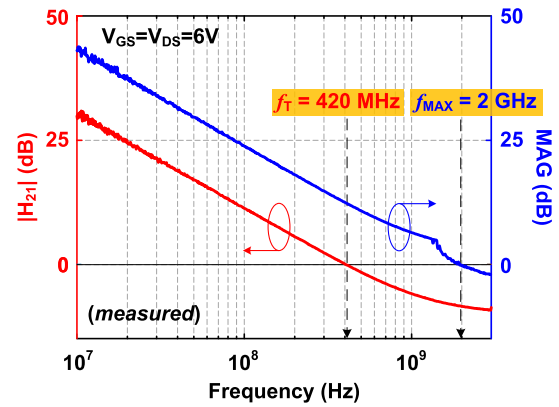

Fig. 13. Measured current gain ($|H_{21}|$) and maximum available power gain (MAG) versus frequency, for a self-aligned ZnO TFT with $W/L = 150/1$ μm (six fingers, each 25 μm wide).

To enhance Q_L, we take advantage of wide metal traces with large cross sections, as well as the low-loss substrates possible in LAE [42], [43], [44], [45] (e.g., tangent loss of ∼0.006 for polyimide and ∼0.005 for Corning glass in LAE versus ∼0.04 for Si substrates in Si-CMOS, at giga-Hertz frequencies). The inset to Fig. 12 shows the inductor, a planar loop of 1 mm radius made with a 0.2 mm wide trace. The loop is made of 2.5 μm-thick thermal-evaporated gold or silver (two metals of low resistivity available in our cleanroom facility). In industrial manufacturing, a thick silver layer can be fabricated using screen printing of nanoparticle ink followed by a short period of annealing to attain high conductivity [46]. EM simulations predict an inductance L_{IND} of ∼4.1 nH, which agrees well with that measured on fabricated inductors via a vector network analyzer (VNA). The measured quality factors at 2.4 GHz are ∼28 for gold and ∼22 for silver. These values are approximately 2.5–3 times that of a monolithic inductor with similar geometry made in Si-CMOS [43], [47].

To raise Q_C, we reduce the gate resistance by building a composite gate electrode stack of Cr/Al/Cr with thicknesses of 10/110/40 nm, as shown in Fig. 6. Its sheet resistance is about 2 $\Omega/\square$.

D. Self-Alignment

Equation (4) suggests that the OFF impedance can be increased by minimizing the S/D-to-G overlap capacitors C_{GS} and C_{GD}. In the standard LAE TFT fabrication process, large C_{GS} and C_{GD} originate from the need to avoid misalignment between source/drain and gate-electrodes [22], [31], [32], [33], [34], [35]. But ensuring adequate alignment margin results in large S/D-to-G overlaps, typically ranging from 10 to 20 μm. We reduce C_{GS} and C_{GD} by using a self-aligned process. When patterning the S/D contacts, we expose the photoresist to UV light incident from the glass substrate side, with the thick gate metal acting as the mask [40]. The self-alignment reliably reduces the overlap down to ∼0.5 μm, correspondingly reducing C_{GS} and C_{GD} tenfold. With the self-alignment technique, as shown in Fig. 13, the unity-current gain frequency f_T and the unity-power gain frequency f_{MAX} for ZnO TFTs are pushed from the mega-Hertz regime to 0.4 and 2 GHz, respectively.
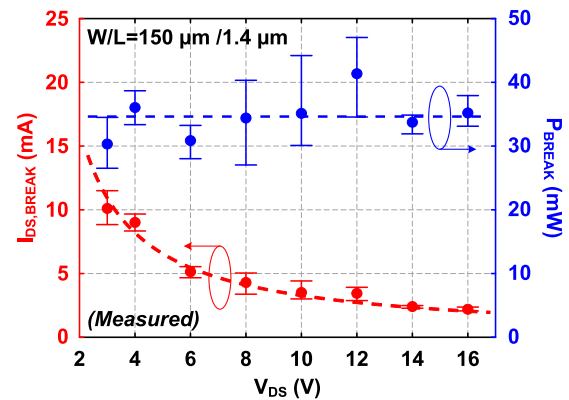
Fig. 14. Measured current $I_{DS,BREAK}$ and power P_{BREAK} ($\triangleq V_{DS} \cdot I_{DS,BREAK}$) over a range of breakdown voltages V_{DS}'s.

E. Aggressive Yet Breakdown-Safe Biasing

Having increased $|Z_{OFF}|$ through resonant operation and TFT self-alignment, we now turn to decreasing the ON-state impedance $|Z_{ON}|$, which is determined by the channel resistance R_{CH} as shown in Fig. 9. In our reconfigurable antenna we use the TFTs as *passive* RF switches that operate in the deep triode regime (i.e., $V_{DS} \ll V_{GS} - V_T$). Therefore, R_{CH} can be approximated as

$$R_{CH} = \frac{1}{\mu_n C_{OX} \frac{W}{L}(V_{GS} - V_T)} \tag{5}$$

where μ_n is the electron mobility and C_{OX} is the gate capacitance per unit area. Raising V_{GS} reduces R_{CH}, but in practice, this is limited by TFT breakdown. Previous work has shown that the safe bias point for employing our TFTs with 40 nm thin gate dielectric, as *active* amplifiers (i.e., $V_{DS} > V_{GS} - V_T$), e.g., in oscillator circuits, is only about 6–8 V [45].

Characterization of the TFT breakdown conditions in Fig. 14 reveals an inverse relationship between V_{DS} and the breakdown current $I_{DS,BREAK}$. The breakdown condition is a roughly constant power P_{BREAK} (defined as $P_{BREAK} \triangleq V_{DS} \cdot I_{DS,BREAK}$). This suggests a thermally induced breakdown mechanism [48], [49], [50].

A key co-design insight is that the antenna architecture employs the TFTs as *passive* switches, rather than as *active*
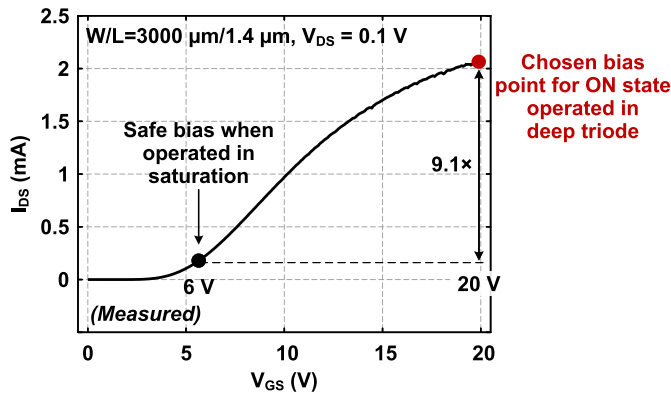
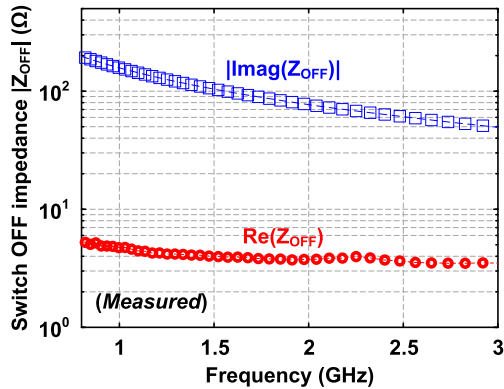Fig. 15. Transfer curve in the deep triode regime of the LAE ZnO TFT used as a passive switch in the antenna.

Fig. 16. Measured OFF-state TFT impedance (without the inductor) versus frequency. The impedance is shown as the real and imaginary parts.
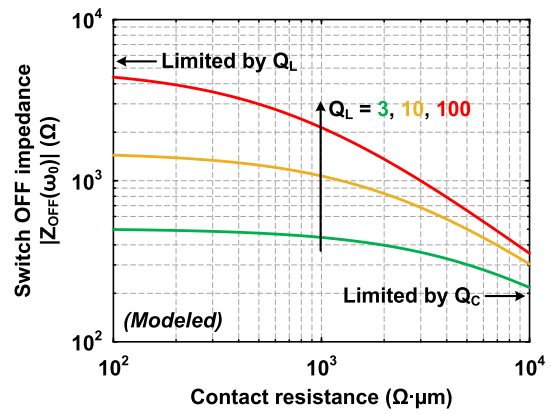

Fig. 17. OFF impedance $|Z_{OFF}(\omega_0)|$ of the resonant switch versus contact resistance (normalized by TFT width), for a range of inductor quality factors Q_L.
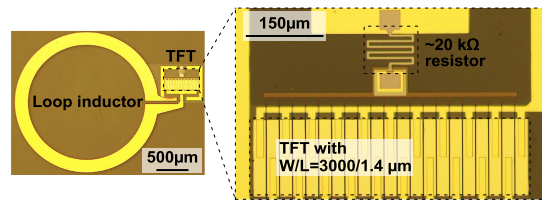
Fig. 18. Die photograph of the LAE resonant RF switch, monolithically fabricated on glass at flex-compatible temperatures ($<$200 °C).

devices. This enables operation in the deep triode regime, with low V_{DS} bias, while active devices require saturation-regime biasing at a much higher V_{DS}. The deep-triode operation reduces TFT power consumption, allowing for increasing V_{GS} from 6–8 to 20 V, while still maintaining an adequate thermal-breakdown margin. The low-V_{DS} transfer curve in Fig. 15 shows that this leads to a 9× reduction in R_{CH}.

F. Limits of the LAE Switch and Outlook

As suggested by (4), the switch OFF impedance is set by the quality factor of the *LC* resonator, i.e., Q_C and Q_L for the capacitor and inductor branches, respectively. In this section, we first analyze the factors that limit Q_C and Q_L in the current LAE technology, and then identify directions for future improvement of switch performance.

As shown in Fig. 16, the real part of the measured OFF-state TFT impedance (without the inductor) is orders of magnitude higher than the gate resistance R_G^L, estimated by $R_G^L = R_\square \cdot ((L + 2L_{OV})/W) \approx 2$ mΩ, where $R_\square = 2$ Ω/$\square$ is the measured gate sheet resistance. This suggests that when we use the thick, composite gate-stack (made of Cr/Al/Cr as shown in Figs. 6 and 8), the OFF impedance is no longer dominated by the gate, but rather possibly by the metal-to-semiconductor contact resistance at the TFT source and drain.

In Fig. 17, we illustrate how the OFF impedance of the resonant switch (with the inductor) scales with contact resistance.

This points out that optimizing the TFT contacts is key to further enhancement of the switch performance. Doping the semiconductor layer [51] or plasma treatment [52] could serve this purpose.

Fig. 17 also suggests that when the contact resistance is minimized down to 100's $\Omega \cdot \mu$m, the inductor quality factor becomes the bottleneck. To address this, layout optimization [53] and integrating ferromagnetic materials [54] are possible solutions.

IV. SYSTEM DEMONSTRATION AND MEASUREMENTS

A. Characterization of the LAE Resonant RF Switch

Combining all the device and circuit techniques of Section III, TFT-based resonant RF switches, as shown in Fig. 18, are fabricated on glass at flex-compatible temperatures ($<$200 °C). A high-impedance $\sim$20 kΩ resistor, made of a 10 nm-thick Cr film, is put in series with the gate. It isolates the dc biasing traces, thereby preventing undesired parasitic RF feedthrough as well as electrostatic discharge (ESD) damage.

Fig. 19 shows the dc transfer curves of our ZnO TFTs and their variations. The measured switch impedance is shown in Fig. 20. Within the band of interest, centered at 2.4 GHz, a $|Z_{OFF}/Z_{ON}|$ of 48 with half-maximum bandwidth of 350 MHz is achieved. The antenna radiation efficiency reaches a maximum at $W/L = 3000/1.4$ μm with $|Z_{OFF}/Z_{ON}| = 48$, which corresponds to a normalized switch size of $\sim$17 in Fig. 4. This device demonstrates, for the first time, an efficient RF switch made in LAE technology, operating in the giga-Hertz frequency regime required for practical wireless systems.

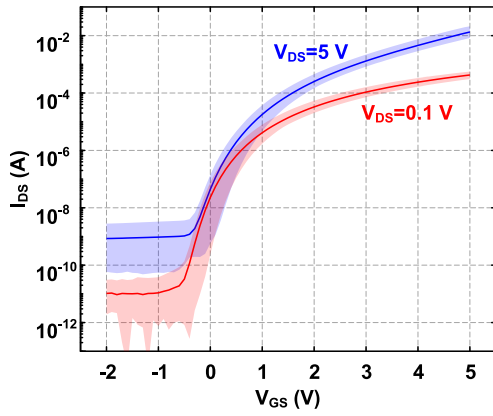Fig. 19. Measured $I_{DS} - V_{GS}$ transfer curves of 15 ZnO TFTs with $W/L = 3000/1.4$ μm at $V_{DS} = 0.1$ and $5V$. The solid line shows an average, while the shaded region shows maximum/minimum boundaries.
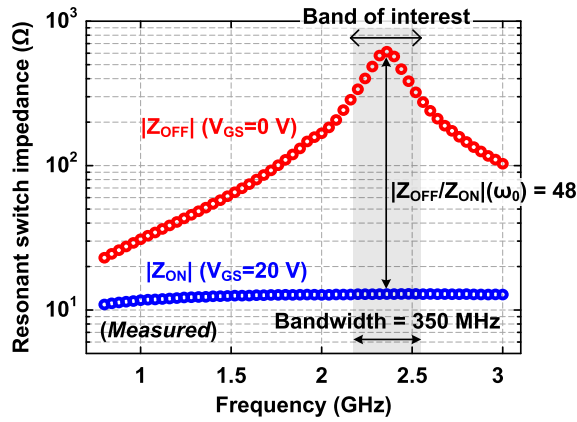

Fig. 20. Measured impedance of the resonant RF switch in the ON and OFF states.

TABLE I
SUMMARY OF TRANSISTOR MEASUREMENTS

S/D-to-G overlap (μm)	~0.5
V_T (V)	3.3±0.2
μ_{FE} (cm^2/V·s)	23±5
SS (mV/dec)	144±15
DC on-off ratio	>3×10^6
Gate leakage	<2.4 fA/μm^2

Table I summarizes the characteristics of the demonstrated LAE TFTs.

B. Antenna Prototype and Measurement Setup

Using the resonant RF switches we now demonstrate the LAE-based reconfigurable antenna. The system prototype is shown in Fig. 21(a). The fabrication techniques employed are fully compatible with the monolithic integration of all components onto a large-area and flexible substrate. Due to the size limitations of our microfabrication equipment, the TFTs are fabricated on a 6×6 cm^2 substrate, diced, and then assembled on a printed circuit board (PCB). This custom PCB carries an aluminum ground plane, a 5 mm-thick dielectric spacer (made of alumina, $\varepsilon_r \approx 9$), the 2-D array of metal patches, and the TFT voltage-supply circuitry. Two dc bias voltages,
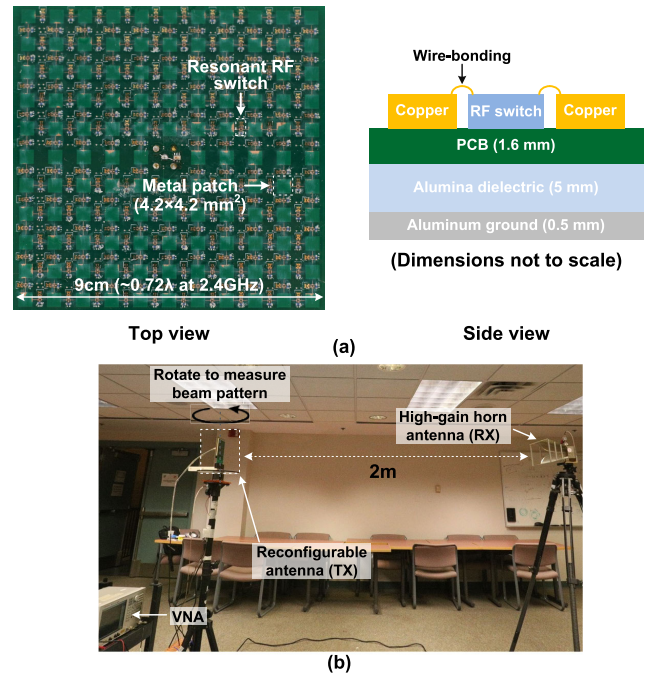

Fig. 21. Antenna (a) prototype, consisting of an 11×11 array of uniformly spaced square metal patches and 208 LAE RF switches, and (b) measurement setup.

0 and 20 V, supplied by two voltage regulators, are pulsed during the measurement to avoid over-stressing the TFTs.

The measurement setup is shown in Fig. 21(b). To identify the antenna's resonant frequency, the reflection coefficient S_{11} is measured by a VNA. To characterize the radiation beam pattern, a horn antenna as the receiver (RX) is placed at $l = 2$ m distance, i.e., in the far-field (defined as $l \gg$ NF, where NF is the near field range of the reconfigurable antenna, estimated as NF $\triangleq (D^2/\lambda) = 6.48$ cm, with aperture size $D = 9$ cm and signal wavelength $\lambda = 12.5$ cm at 2.4 GHz). The radiated signal from the reconfigurable antenna as the transmitter (TX) is measured while it is rotated in steps of $1.8°$. A high-gain RX antenna (gain = 18) is used to minimize indoor multipath interference.

C. Prototype Measurements

Test results of the antenna's reconfigurability in the beam direction are shown in Fig. 22. By changing the switch configuration, while maintaining the same resonant frequency, the beam is steered from $0°$ to $-35°$ and $55°$, covering a $90°$ steering range. This directional reconfigurability will enable spatial addressing of densely distributed sensors, as illustrated in Fig. 1. A better spatial resolution, i.e., a narrower beam, can be realized by increasing the antenna's aperture size, as the beamwidth inversely scales with the aperture size [37].

We also test reconfigurability in the frequency domain. The results shown in Fig. 23 are obtained while the beam direction is maintained at $0°$. It is seen that the resonant frequency is shifted from 2.4 to 2.2 GHz, demonstrating a 200 MHz frequency tuning range. With typical 5 MHz frequency spacing, in the 2.4 GHz band this tuning range can accommodate forty channels, enabling dynamic spectrum allocation. This also enables frequency division multiplexing

TABLE II
SUMMARY AND COMPARISON OF PROTOTYPE MEASUREMENTS

	This work	[8]	[9]	[13]	[14]	[15]	[16]
Technology	LAE	Discrete Si BJT	Discrete Si diode	RF MEMS	Discrete III-V varactor	Discrete Si PIN diode	Discrete Si PIN diode
Full-aperture monolithically-integrable over large dimension	Yes	No	No	No	No	No	No
Capable of flexible form factor	Yes	No	No	No	No	No	No
Size of aperture (wavelength)	0.72λ × 0.72λ	0.8λ × 0.8λ	0.72λ × 0.72λ	0.5λ × 0.5λ	0.9λ × 0.3λ	0.72λ × 0.7λ	0.3λ × 0.9λ
Size of aperture (cm)	9 × 9	22.5 × 22	8.7 × 8.7	2.5 × 2.5	10.7 × 4.1	4.3 × 4.2	2.6 × 8.3
Frequency (GHz)	2.1-2.5	0.8-1.5	2.4-3.0	5.7-8.2	2.15-2.38	4.9-5.1	3.3-3.5
Antenna efficiency	33%	63%*	-	-	41%-87%	81%*	70%*
Static power of switch-control	<5 µW	~10 mW	0.42 W	-	-	78 mW	35.6 mW
Steering range (°)	90	90	60	28	46	80	31
Average Half Power Beam Width (HPBW) (°)	72	76	50	94	51.2	70	105

**The antenna efficiency does not include the significant static power of switch-control.*

(a)

(b)

(c)
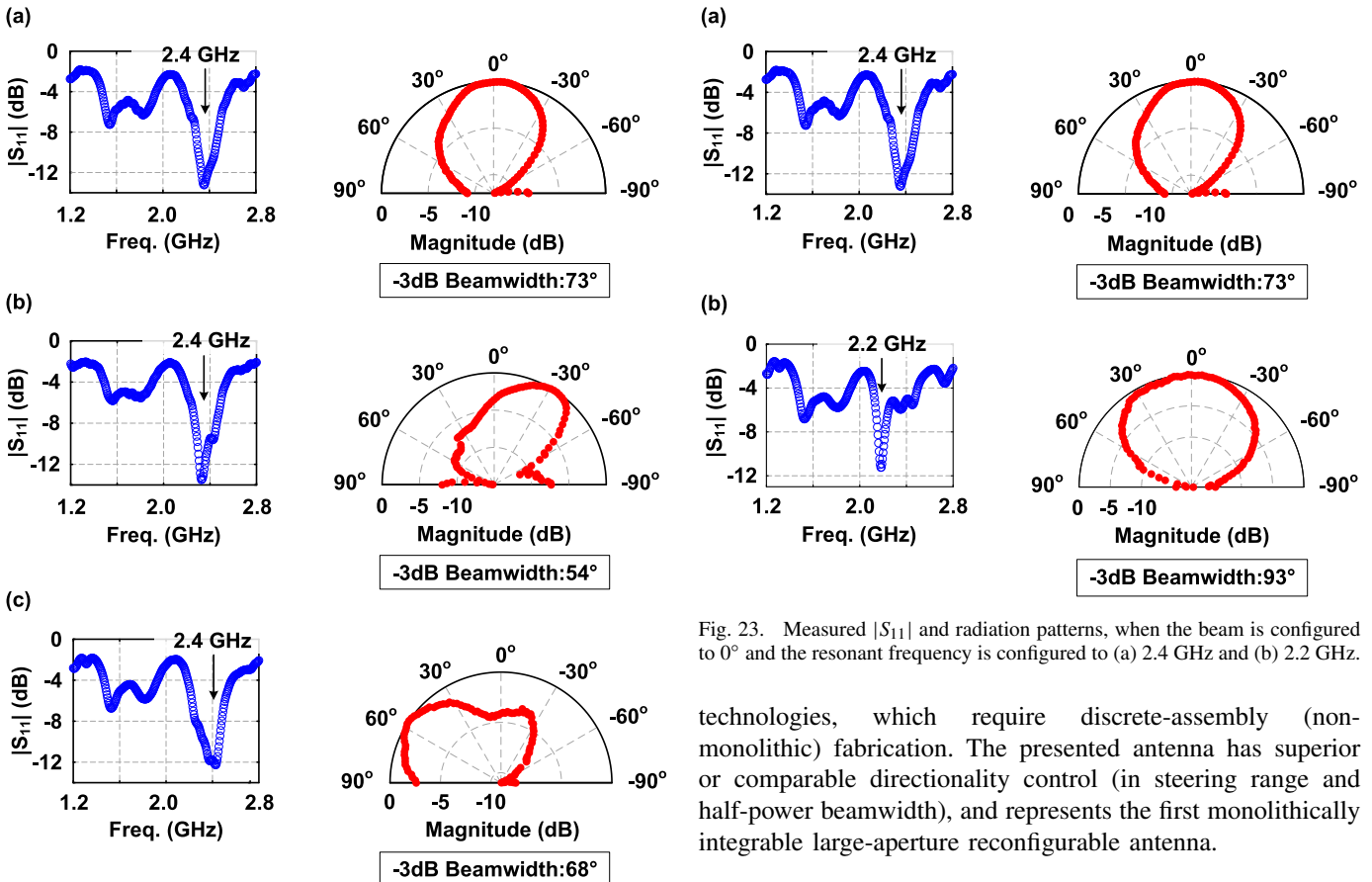
Fig. 22. Measured $|S_{11}|$ and radiation patterns, when the resonant frequency is configured to 2.4 GHz and the beam is configured to (a) 0°, (b) −35°, and (c) 55°.

to enhance the signal-to-noise ratio (SNR) in IoT wireless systems [5], [7].

Table II summarizes the characteristics of the present antenna prototype, and those of previously reported reconfigurable antennas based on Si, RF-MEMS, and III–V

(a)

(b)

Fig. 23. Measured $|S_{11}|$ and radiation patterns, when the beam is configured to 0° and the resonant frequency is configured to (a) 2.4 GHz and (b) 2.2 GHz.

technologies, which require discrete-assembly (non-monolithic) fabrication. The presented antenna has superior or comparable directionality control (in steering range and half-power beamwidth), and represents the first monolithically integrable large-aperture reconfigurable antenna.

V. CONCLUSION

Giga-Hertz RF switches in LAE technology were achieved by co-designing device, circuit, and architecture for a large-area reconfigurable antenna. The LAE RF switches enable the first-time demonstration of a monolithically integrable, large-aperture reconfigurable antenna for 2.4 GHz wireless systems. Dynamically tunable resonant frequency and radiation patterns were realized and measured. This work

demonstrates the feasibility of LAE as a technology for future IoT wireless systems.

While this work demonstrates the feasibility of LAE systems for emerging RF applications, opening up new capabilities toward large-aperture-enabled performance and agility, we see many avenues for further progress, from the technology through to its applications.

On the technological level, large-area thin-film semiconductors have seen steady progress in critical materials properties, such as mobility [20], [55], [56]. This progress holds the promise of enabling higher frequency and/or higher power handling, leading to increased and higher-performance RF functionality. At the device level, this work has exposed the frequency-limiting parameters, such as S/D contact resistance and S/D-to-G overlap capacitance. We see substantial opportunities to address these limitations through structural and processing optimizations. Finally, we see opportunities for features beyond the devices, such as for enhanced thermal dissipation [57], [58], to extend device operation beyond the thermal-breakdown limits seen today, especially on thermally insulating substrates such as glass and plastic.

At the system level, we anticipate many new wireless system concepts to emerge. But even for reconfigurable antennas such as those presented, we see opportunities for optimizing geometric array design. Such optimization could address particular far-field characteristics/targets, work together with various, dynamic shapes afforded by antenna conformality, and be designed for various RF driver architectures and attributes. Finally, arranging multiple reconfigurable antennas in an array (e.g., a phased array) presents an interesting avenue [59]. The single-element reconfigurability can be utilized to increase the overall gain factor, mitigate grating lobes, and avoid aliasing in sparse arrays.

At the application level, research on control algorithms is essential. So far, analyzing reconfigurable antennas, specifically the mapping of switch configuration to output radiation characteristics, relies on time-consuming EM simulation. As LAE has now pushed reconfigurable antennas into an unprecedented design space, wherein degrees of control are greatly expanded (e.g., 2^{208} in this work), undertaking exhaustive analysis of each configuration becomes infeasible. This will make efficient models for inverse design critical, along with the integration of such models in larger control systems that drive the optimal radiation patterns desired for sensing and communication tasks.

REFERENCES

[1] F. Mattern and C. Floerkemeier, "From the Internet of Computers to the Internet of Things," in *From Active Data Management to Event-Based Systems and More*. Cham, Switzerland: Springer, Mar. 2010, pp. 242–259.

[2] C. Perera, A. Zaslavsky, P. Christen, and D. Georgakopoulos, "Context aware computing for the Internet of Things: A survey," *IEEE Commun. Surveys Tuts.*, vol. 16, no. 1, pp. 414–454, 1st Quart., 2014.

[3] C. X. Mavromoustakis, G. Mastorakis, and J. M. Batalla, *Internet of Things (IoT) in 5G Mobile Technologies*. Cham, Switzerland: Springer, 2016.

[4] M. A. Matin, *Wideband, Multiband, and Smart Reconfigurable Antennas for Modern Wireless Communications*. Hershey, PA, USA: IGI Global, 2015.

[5] C. G. Christodoulou, Y. Tawk, S. A. Lane, and S. R. Erwin, "Reconfigurable antennas for wireless and space applications," *Proc. IEEE*, vol. 100, no. 7, pp. 2250–2261, Jul. 2012.

[6] J. Costantine, Y. Tawk, S. E. Barbin, and C. G. Christodoulou, "Reconfigurable antennas: Design and applications," *Proc. IEEE*, vol. 103, no. 3, pp. 424–437, Mar. 2015.

[7] J. T. Bernhard, *Reconfigurable Antennas*. Cham, Switzerland: Springer, 2007.

[8] L. N. Pringle et al., "A reconfigurable aperture antenna based on switched links between electrically small metallic patches," *IEEE Trans. Antennas Propag.*, vol. 52, no. 6, pp. 1434–1445, Jun. 2004.

[9] D. Rodrigo, B. A. Cetiner, and L. Jofre, "Frequency, radiation pattern and polarization reconfigurable antenna using a parasitic pixel layer," *IEEE Trans. Antennas Propag.*, vol. 62, no. 6, pp. 3422–3427, Jun. 2014.

[10] G. H. Huff and J. T. Bernhard, "Integration of packaged RF MEMS switches with radiation pattern reconfigurable square spiral microstrip antennas," *IEEE Trans. Antennas Propag.*, vol. 54, no. 2, pp. 464–469, Feb. 2006.

[11] Y. Tawk, A. R. Albrecht, S. Hemmady, G. Balakrishnan, and C. G. Christodoulou, "Optically pumped frequency reconfigurable antenna design," *IEEE Antennas Wireless Propag. Lett.*, vol. 9, pp. 280–283, 2010.

[12] B. Kim, B. Pan, S. Nikolaou, Y.-S. Kim, J. Papapolymerou, and M. M. Tentzeris, "A novel single-feed circular microstrip antenna with reconfigurable polarization capability," *IEEE Trans. Antennas Propag.*, vol. 56, no. 3, pp. 630–638, Mar. 2008.

[13] C. Jung, M. Lee, G. P. Li, and F. DeFlaviis, "Reconfigurable scan-beam single-arm spiral antenna integrated with RF-MEMS switches," *IEEE Trans. Antennas Propag.*, vol. 54, no. 2, pp. 455–463, Feb. 2006.

[14] S. N. M. Zainarry, N. Nguyen-Trong, and C. Fumeaux, "A frequency- and pattern-reconfigurable two-element array antenna," *IEEE Antennas Wireless Propag. Lett.*, vol. 17, no. 4, pp. 617–620, Apr. 2018.

[15] S. Tang, Y. Zhang, Z. Han, C.-Y. Chiu, and R. Murch, "A pattern-reconfigurable antenna for single-RF 5G millimeter-wave communications," *IEEE Antennas Wireless Propag. Lett.*, vol. 20, no. 12, pp. 2344–2348, Dec. 2021.

[16] W.-Q. Deng, X.-S. Yang, C.-S. Shen, J. Zhao, and B.-Z. Wang, "A dual-polarized pattern reconfigurable Yagi patch antenna for microbase stations," *IEEE Trans. Antennas Propag.*, vol. 65, no. 10, pp. 5095–5102, Oct. 2017.

[17] M. Poveda-Garcia, A. G. Martinez, and J. L. Gomez-Tornero, "Frequency-scanned focused leaky-wave antennas for direction-of-arrival detection in proximity BLE sensing applications," in *Proc. 14th Eur. Conf. Antennas Propag. (EuCAP)*, Mar. 2020, pp. 1–4.

[18] P. P. Mercier, S. Bandyopadhyay, A. C. Lysaght, K. M. Stankovic, and A. P. Chandrakasan, "A sub-nW 2.4 GHz transmitter for low data-rate sensing applications," *IEEE J. Solid-State Circuits*, vol. 49, no. 7, pp. 1463–1474, Jul. 2014.

[19] K. Shafique et al., "Energy harvesting using a low-cost rectenna for Internet of Things (IoT) applications," *IEEE Access*, vol. 6, pp. 30932–30941, 2018.

[20] K. Myny, "The development of flexible integrated circuits based on thin-film transistors," *Nature Electron.*, vol. 1, no. 1, pp. 30–39, Jan. 2018.

[21] K. Nomura, H. Ohta, A. Takagi, T. Kamiya, M. Hirano, and H. Hosono, "Room-temperature fabrication of transparent flexible thin-film transistors using amorphous oxide semiconductors," *Nature*, vol. 432, no. 7016, pp. 488–492, Nov. 2004.

[22] S. R. Forrest, "The path to ubiquitous and low-cost organic electronic appliances on plastic," *Nature*, vol. 428, no. 6986, pp. 911–918, Apr. 2004.

[23] M. Kaltenbrunner et al., "An ultra-lightweight design for imperceptible plastic electronics," *Nature*, vol. 499, no. 7459, pp. 458–465, 2013.

[24] G. Shaker, S. Safavi-Naeini, N. Sangary, and M. M. Tentzeris, "Inkjet printing of ultrawideband (UWB) antennas on paper-based substrates," *IEEE Antennas Wireless Propag. Lett.*, vol. 10, pp. 111–114, 2011.

[25] T. Someya, T. Sekitani, S. Iba, Y. Kato, H. Kawaguchi, and T. Sakurai, "A large-area, flexible pressure sensor matrix with organic field-effect transistors for artificial skin applications," *Proc. Nat. Acad. Sci. USA*, vol. 101, no. 27, pp. 9966–9970, Jul. 2004.

[26] N. Papadopoulos et al., "Touchscreen tags based on thin-film electronics for the Internet of Everything," *Nature Electron.*, vol. 2, no. 12, pp. 606–611, Dec. 2019.

[27] T. Sekitani et al., "A large-area wireless power-transmission sheet using printed organic transistors and plastic MEMS switches," *Nature Mater.*, vol. 6, no. 6, pp. 413–417, Jun. 2007.

[28] R. H. Reuss et al., "Macroelectronics: Perspectives on technology and applications," *Proc. IEEE*, vol. 93, no. 7, pp. 1239–1256, Jul. 2005.

[29] B. Salgado and C. Xie. *Corning Celebrates Grand Opening of Gen 10.5 LCD Glass Plant in Wuhan, China.* Accessed: Jan. 16, 2023. [Online]. Available: https://www.corning.com/worldwide/en/products/display-glass/resources/thought-leadership/corning-celebrates-opening-of-new-gen-10-5-lcd-glass-substrate-f.html

[30] F. De Roose et al., "A flexible thin-film pixel array with a charge-to-current gain of $59\mu A/pC$ and 0.33% nonlinearity and a cost effective readout circuit for large-area X-ray imaging," in *IEEE Int. Solid-State Circuits Conf. (ISSCC) Dig. Tech. Papers*, Jan. 2016, pp. 296–297.

[31] K. Myny et al., "Plastic circuits and tags for 13.56 MHz radio-frequency communication," *Solid. State. Electron.*, vol. 53, no. 12, pp. 1220–1226, 2009.

[32] J. S. Park, W.-J. Maeng, H.-S. Kim, and J.-S. Park, "Review of recent developments in amorphous oxide semiconductor thin-film transistor devices," *Thin Solid Films*, vol. 520, no. 6, pp. 1679–1693, Jan. 2012.

[33] L. Huang et al., "A super-regenerative radio on plastic based on thin-film transistors and antennas on large flexible sheets for distributed communication links," in *IEEE Int. Solid-State Circuits Conf. (ISSCC) Dig. Tech. Papers*, Feb. 2013, pp. 458–459.

[34] T. Moy et al., "An EEG acquisition and biomarker-extraction system using low-noise-amplifier and compressive-sensing circuits based on flexible, thin-film electronics," *IEEE J. Solid-State Circuits*, vol. 52, no. 1, pp. 309–321, Jan. 2017.

[35] C. Wu et al., "Gigahertz large-area-electronics RF switch and its application to reconfigurable antennas," in *Int. Electron Devices Meeting Tech. Dig.*, Dec. 2020, pp. 33.6.1–33.6.4.

[36] *CST Microwave Studio.* Accessed: Jan. 16, 2023. [Online]. Available: https://www.3ds.com/

[37] C. A. Balanis, *Antenna Theory: Analysis and Design*, 3rd ed. Hoboken, NJ, USA: Wiley, 2005.

[38] D. A. Mourey, D. A. Zhao, and T. N. Jackson, "ZnO thin film transistors and circuits on glass and polyimide by low-temperature PEALD," in *Int. Electron Devices Meeting Tech. Dig.*, Dec. 2009, pp. 8.5.1–8.5.4.

[39] L. Lu, J. Li, H. S. Kwok, and M. Wong, "High-performance and reliable elevated-metal metal-oxide thin-film transistor for high-resolution displays," in *Int. Electron Devices Meeting Tech. Dig.*, Dec. 2016, pp. 32.2.1–32.2.4.

[40] Y. Mehlman, Y. Afsar, N. Yerma, S. Wagner, and J. C. Sturm, "Self-aligned ZnO thin-film transistors with 860 MHz f_T and 2 GHz f_{max} for large-area applications," in *Proc. 75th Annu. Device Res. Conf. (DRC)*, Jun. 2017, pp. 1–2.

[41] M. Chen, Y. Miao, Y. Hao, and K. Hwang, "Narrow band Internet of Things," *IEEE Access*, vol. 5, pp. 20557–20577, 2017.

[42] C. Wu et al., "A phased array based on large-area electronics that operates at gigahertz frequency," *Nature Electron.*, vol. 4, no. 10, pp. 757–766, Oct. 2021.

[43] D. S. Gardner, G. Schrom, F. Paillet, B. Jamieson, T. Karnik, and S. Borkar, "Review of on-chip inductor structures with magnetic films," *IEEE Trans. Magn.*, vol. 45, no. 10, pp. 4760–4766, Oct. 2009.

[44] Y. Hu et al., "A self-powered system for large-scale strain sensing by combining CMOS ICs with large-area electronics," *IEEE J. Solid-State Circuits*, vol. 49, no. 4, pp. 838–850, Apr. 2014.

[45] Y. Afsar, T. Moy, N. Brady, S. Wagner, J. C. Sturm, and N. Verma, "15.1 Large-scale acquisition of large-area sensors using an array of frequency-hopping ZnO thin-film-transistor oscillators," in *IEEE Int. Solid-State Circuits Conf. (ISSCC) Dig. Tech. Papers*, Feb. 2017, pp. 258–260.

[46] W. Gu et al., "Fast near infrared sintering of silver nanoparticle ink and applications for flexible hybrid circuits," *RSC Adv.*, vol. 8, no. 53, pp. 30215–30222, 2018.

[47] J. N. Burghartz and B. Rejaei, "On the design of RF spiral inductors on silicon," *IEEE Trans. Electron Devices*, vol. 50, no. 3, pp. 718–729, Mar. 2003.

[48] Y. Mehlman, P. Kumar, M. Ozatay, S. Wagner, J. C. Sturm, and N. Verma, "Large-area electronics HF RFID reader array for object-detecting smart surfaces," *IEEE Solid-State Circuits Lett.*, vol. 1, no. 8, pp. 182–185, Aug. 2018.

[49] S. Urakawa et al., "Thermal analysis of amorphous oxide thin-film transistor degraded by combination of Joule heating and hot carrier effect," *Appl. Phys. Lett.*, vol. 102, no. 5, Feb. 2013, Art. no. 053506.

[50] S.-W. Lee et al., "Abnormal output characteristics of p-type low temperature polycrystalline silicon thin film transistor fabricated on polyimide substrate," *IEEE J. Electron Devices Soc.*, vol. 4, no. 1, pp. 7–10, Jan. 2016.

[51] P. S. Yun and J. Koike, "Metal reaction doping and ohmic contact with Cu-Mn electrode on amorphous In-Ga-Zn-O semiconductor," *J. Electrochem. Soc.*, vol. 158, no. 10, p. H1034, 2011.

[52] S. Knobelspies, A. Takabayashi, A. Daus, G. Cantarella, N. Münzenrieder, and G. Tröster, "Improvement of contact resistance in flexible a-IGZO thin-film transistors by CF_4/O_2 plasma treatment," *Solid-State Electron.*, vol. 150, pp. 23–27, Dec. 2018.

[53] J. M. Lopez-Villegas, J. Samitier, C. Cane, P. Losantos, and J. Bausells, "Improvement of the quality factor of RF integrated inductors by layout optimization," *IEEE Trans. Microw. Theory Techn.*, vol. 48, no. 1, pp. 76–83, Mar. 2000.

[54] H. Wu, S. Zhao, D. S. Gardner, and H. Yu, "Improved high frequency response and quality factor of on-chip ferromagnetic thin film inductors by laminating and patterning Co-Zr-Ta-B films," *IEEE Trans. Magn.*, vol. 49, no. 7, pp. 4176–4179, Jul. 2013.

[55] T. Kamiya, K. Nomura, and H. Hosono, "Present status of amorphous In–Ga–Zn–O thin-film transistors," *Sci. Technol. Adv. Mater.*, vol. 11, no. 4, Feb. 2010, Art. no. 044305.

[56] Y. Ma, C. Wu, Y. Mehlman, S. Wagner, N. Verma, and J. C. Sturm, "Material aspects of giga-Hertz ZnO TFTs for wireless systems," *MRS Adv.*, vol. 7, nos. 13–14, pp. 265–272, May 2022.

[57] Y. Ma et al., "Device, circuit, and system design for enabling giga-Hertz large-area electronics," *IEEE Open J. Solid-State Circuits Soc.*, vol. 2, pp. 177–192, 2022.

[58] P.-Y. Liao et al., "Transient thermal and electrical co-optimization of BEOL top-gated ALD In_2O_3 FETs toward monolithic 3-D integration," *IEEE Trans. Electron Devices*, vol. 70, no. 4, pp. 2052–2058, Apr. 2023.

[59] T. L. Roach, G. H. Huff, and J. T. Bernhard, "On the applications for a radiation reconfigurable antenna," in *Proc. 2nd NASA/ESA Conf. Adapt. Hardw. Syst. (AHS)*, Aug. 2007, pp. 7–13.

Can Wu (Student Member, IEEE) received the B.S. degree from the Institute of Microelectronics, Tsinghua University, Beijing, China, in 2013, and the M.A. and Ph.D. degrees in electrical and computer engineering from Princeton University, Princeton, NJ, USA, in 2016 and 2021, respectively.

He is currently a Post-Doctoral Research Fellow with Stanford University, Stanford, CA, USA. His research interests include giga-Hertz large-area thin-film electronics, wireless sensing, wearable and implantable devices, and bioelectronics.

Dr. Wu is a recipient of the Best Student Poster Award at 2015 Flex Conference, the Best Student Paper Award at 2019 Device Research Conference, and the Princeton University Gordon Wu Fellowship.

Yue Ma (Graduate Student Member, IEEE) received the B.S. degree in physics from Nanjing University, Nanjing, China, in 2018, and the M.A. degree in electrical engineering from Princeton University, Princeton, NJ, USA, in 2020, where he is currently pursuing the Ph.D. degree in electrical and computer engineering.

He worked as a summer Research Intern with the University of California at Los Angeles, Los Angeles, CA, USA, in 2017. He has previously completed an internship in product RF definition at Apple Inc., Cupertino, CA, USA, in the summer of 2022. His research interests include the co-design of device, circuit, and systems based on gigahertz large-area electronics.

Suresh Venkatesh (Senior Member, IEEE) received the M.S. degree in electrical and computer engineering from North Carolina State University, Raleigh, NC, USA, in 2010, and the Ph.D. degree in electrical and computer engineering from the University of Utah, Salt Lake City, UT, USA, in 2017.

He is currently an Assistant Professor with North Carolina State University, Electrical and Computer Engineering Department. Prior to joining NC State, he was an Associate Research Scholar with the Electrical and Computer Engineering Department, Princeton University, Princeton, NJ, USA. He was also a Research Project Assistant with Molecular Astronomy Laboratory, Raman Research Institute, Bangalore during 2007–2008, where he worked on millimeter-wave radio telescope. He has authored/coauthored more than 60 journal and conference publications. His research interests are in electromagnetics, metamaterials, antenna design, integrated circuits, computational imaging, and transformation optics design.

Dr. Venkatesh is an Affiliate Member of MTT-23 Wireless Communication and MTT-21 Terahertz Technology and Applications committees. His Ph.D. dissertation received the Electrical and Computer Engineering (ECE) Outstanding Dissertation Award, 2016. He was a recipient of the 2021 Mistletoe Research Fellowship from Momental Foundation. He also served as the IEEE MTTS YP Region 1–6 coordinator and as a committee member at the Climate and Inclusion Committee, ECE Princeton University.

Yoni Mehlman (Student Member, IEEE) received the Ph.D. degree in electrical engineering from Princeton University, Princeton, NJ, USA, in 2020.

His doctoral studies focused on the scaling of thin-film transistors to enhance their high-frequency performance for novel RF applications. He is currently works at Tower Semiconductor for the Mixed Signal and Power Management Group, where he is responsible for developing the next generation of integrated power MOSFETs. His research interests include device and process engineering to enhance beyond-breakdown voltage (BV) laterally diffused metal–oxide semiconductor (LDMOS) characteristics.

Murat Ozatay (Member, IEEE) received the B.Sc. degree in electrical and electronics engineering from Middle East Technical University, Ankara, Turkey, in 2015, and the M.A. degree in electrical engineering from Princeton University, Princeton, NJ in 2017, where he is currently pursuing the Ph.D. degree.

His research focuses on bringing together algorithms and insights for learning with technologies and systems for advanced sensing. His primary research interests include machine learning, artificial intelligence, Internet-of-Things, and the design of very-large-scale integration systems.

Sigurd Wagner (Life Fellow, IEEE) received the Ph.D. degree in physical chemistry from the University of Vienna, Vienna, Austria, in 1968.

Following a Post-Doctoral Fellowship with The Ohio State University, Columbus, OH, USA, he worked with the Bell Telephone Laboratories in Murray Hill and Holmdel, NJ, USA, from 1970 to 1978, on semiconductor memories and heterojunction solar cells. He then joined the Solar Energy Research Institute [currently, National Renewable Energy Laboratory (NREL)], Golden, CO, USA, as the Founding Chief of the Photovoltaic Research Branch. He has been a Professor of Electrical Engineering with Princeton University, Princeton, NJ, USA, since 1980; and in 2015, he became a Professor Emeritus and a Senior Scholar. He has been developing fundamentally new materials, processes, and components for flexible large-area electronics, electrotextiles, and electronic skin, and is considered the father of soft elastic electronics.

Dr. Wagner received the Nevill Mott Prize for his groundbreaking research, both fundamental and applied, on amorphous semiconductors and chalcopyrites, and the International Thin-Film Transistor Conference (ITC) Anniversary Prize for pioneering research on flexible and stretchable large-area electronics, and the comprehensive study of its mechanical behavior. He is a Fellow of the American Physical Society and a member of the Austrian Academy of Science. He is also a member of Princeton's Large-area Systems Group whose goal is to demonstrate complete large-area applications based on hybrid thin-film/CMOS architectures.

James C. Sturm (Life Fellow, IEEE) was born in Berkeley Heights, NJ, USA, in 1957. He received the B.S.E. degree in electrical engineering and engineering physics from Princeton University, Princeton, NJ, USA, in 1979, and the M.S.E.E. and Ph.D. degrees from Stanford University, Stanford, CA, USA, in 1981 and 1985, respectively.

He joined Intel Corporation, Santa Clara, CA, USA, in 1979, as a Microprocessor Design Engineer, and he was a Visiting Engineer with Siemens, Munich, Germany, in 1981. He joined the Faculty of Princeton University, in 1986, where he is currently the Stephen R. Forrest Professor of Electrical Engineering. He has worked in the fields of silicon-based heterojunctions, thin-film and flexible electronics, photovoltaics, the nano-bio interface, 3-D integration, and silicon-on-insulator.

Dr. Sturm is a member of the National Academy of Inventors. He has won over ten awards for teaching excellence and was a National Science Foundation Presidential Young Investigator. He has been active in the leadership of the Device Research Conference, International Electron Devices Meeting, Materials Research Society, and International SiGe Technology and Device Meeting. He co-founded Aegis Lightwave and SpaceTouch.

Naveen Verma (Senior Member, IEEE) received the B.A.Sc. degree in electrical and computer engineering from the University of British Columbia, Vancouver, BC, Canada, in 2003, and the M.S. and Ph.D. degrees in electrical engineering from the Massachusetts Institute of Technology, Cambridge, MA, USA, in 2005 and 2009, respectively.

He has been with Princeton University, Princeton, NJ, USA, since July 2009, where he is a current Director of the Keller Center for Innovation in Engineering Education and a Professor of Electrical and Computer Engineering. His research focuses on advanced sensing systems, exploring how systems for learning, inference, and action planning can be enhanced by algorithms that exploit new sensing and computing technologies. This includes research on large-area, flexible sensors, energy-efficient statistical-computing architectures and circuits, and machine-learning and statistical-signal-processing algorithms.

Dr. Verma is a recipient of numerous teaching and research awards, including several best-paper awards, with his students. He has served as a Distinguished Lecturer for the IEEE Solid-State Circuits Society, and for a number of conference program committees and advisory groups.